Enhancement of ultrafast demagnetization rate and Gilbert damping driven by femtosecond laser-induced spin currents in $Fe_{81}Ga_{19}/Ir_{20}Mn_{80}$ bilayers

Wei Zhang,[1,2] Qian Liu,[3] Zhe Yuan,[3] Ke Xia,[3] Wei He,[1] Qing-feng Zhan,[4] Xiang-qun Zhang,[1] and Zhao-hua Cheng[1,2,5,*]

[1]*State Key Laboratory of Magnetism and Beijing National Laboratory for Condensed Matter Physics, Institute of Physics, Chinese Academy of Sciences, Beijing 100190, China*

[2]*School of Physical Sciences, University of Chinese Academy of Sciences, Beijing 100049, China*

[3]*The Center for Advanced Quantum Studies and Department of Physics, Beijing Normal University, Beijing 100875, China*

[4]*State Key Laboratory of Precision Spectroscopy, School of Physics and Materials Science, East China Normal University, Shanghai 200241, China*

[5]*Songshan Lake Materials Laboratory, Dongguan, Guangdong 523808, China*

(Received 24 October 2018; revised manuscript received 19 July 2019; published 9 September 2019)

In spintronics applications, ultrafast spin dynamics have to be controlled at femtosecond timescales via femtosecond laser radiation. At such ultrafast timescales, the effect of the Gilbert damping factor α on ultrafast demagnetization time τ_M should be considered. In previous explorations for the relationship between these two parameters, it was found that the theoretical calculations based on the local spin-flip scattering model do not agree with the experimental results. Here, we find that in $Fe_{81}Ga_{19}$(FeGa)/$Ir_{20}Mn_{80}$(IrMn) bilayers, the unconventional IrMn thickness dependence of α results from the competition between spin currents pumped from the ferromagnetic (FM) FeGa layer to the antiferromagnetic (AFM) IrMn layer and those pumped from the AFM layer to the FM layer. More importantly, we establish a proportional relationship between the change of the ultrafast demagnetization rate and the enhancement of Gilbert damping induced by the spin currents via interfacial spin chemical potential μ_s. Our work builds a bridge to connect the ultrafast demagnetization time and Gilbert damping in ultrafast photoinduced spin-current-dominated systems, which not only explains the disagreement between experimental and theoretical results in the relation of τ_M with α but provides further insight into ultrafast spin dynamics as well.

DOI: 10.1103/PhysRevB.100.104412

I. INTRODUCTION

The understanding of spin dynamics from nanosecond down to femtosecond timescales is an essential task towards the realization of ultrafast spintronic devices in the frequency range from gigahertz to terahertz [1,2]. The study of ultrafast demagnetization time τ_M is one of the most challenging problems in laser-induced ultrafast spin dynamics. The Gilbert damping factor α is of the utmost importance for high-frequency switching of spintronic devices. Since both τ_M and α require a transfer of angular momentum from the electronic system to the lattice, the unification of these two seemingly unrelated parameters can facilitate the exploration of the microscopic mechanism of laser-induced ultrafast spin dynamics. An inversely proportional relationship between τ_M and α was predicted by theoretical calculations based on the local phonon-mediated Elliott-Yafet scattering mechanism [3–5] as well as the stochastic Landau-Lifshitz-Bloch (LLB) model [6]. However, the relationship between τ_M and α has been debated for over one decade [7]. Until now, all experimental results have shown that τ_M increases with α [8–12].

Apart from the local spin-flip scattering mechanism [13], we proposed that the nonlocal spin currents should be taken into account to coordinate the contradiction in the relationship between τ_M and α. Previous work suggested that the superdiffusive spin current contributed to ultrafast demagnetization [14], while the Gilbert damping could also be enhanced via nonlocal spin currents in ferromagnetic (FM)/nonmagnetic (NM) [15] and FM/antiferromagnetic (AFM) heterostructures [16]. Femtosecond laser irradiation of ferromagnetic thin films is a fascinating novel approach to create large spin currents [17,18]. Figure 1(a) shows that in the case of time-resolved magneto-optical Kerr effect (TRMOKE) experiments, hot electrons excited by femtosecond laser pulses can travel at high velocities and over tens of nanometers through the films. The difference of mean free path between spin-majority and spin-minority hot electrons in ferromagnetic thin films generates superdiffusive spin currents on femtosecond timescales. Such spin currents dissipated at the interface of the heterostructure result in the out-of-equilibrium spin accumulation represented by spin chemical potential μ_s. Moreover, Fig. 1(b) shows that the damped magnetization precession around the effective field could be influenced via spin current. Tveten *et al.* [19] predicted that the ultrafast demagnetization time τ_M could be described in the language of spin-current-induced damping α_{sp} in magnetic heterostructures based on the electron-magnon scattering theory. However, the experimental evidence on the connection of ultrafast demagnetization time with damping driven by femtosecond laser-induced spin currents is not yet understood.

*To whom all correspondence should be addressed: zhcheng@iphy.ac.cn

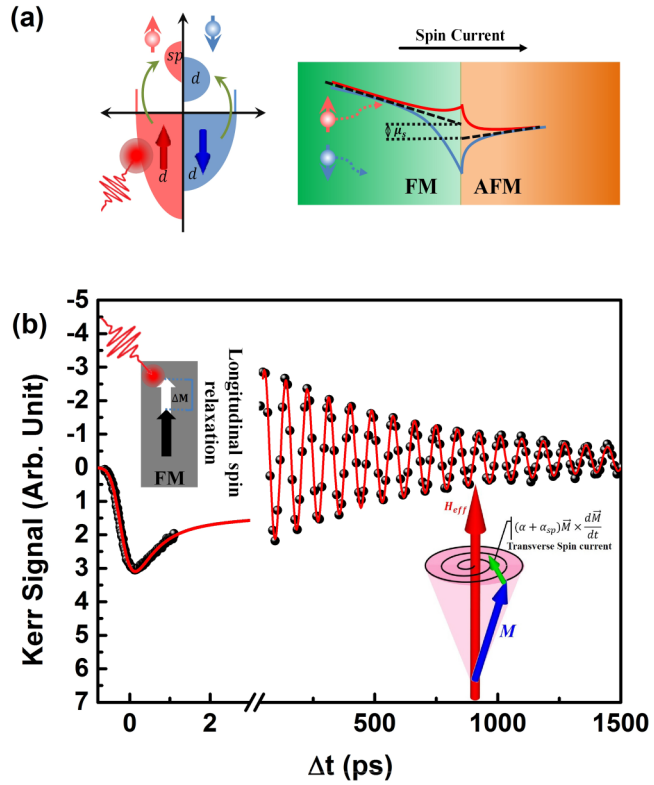

FIG. 1. Basic concept of both ultrafast demagnetization and spin precession induced by spin currents. (a) The excitation of femtosecond laser pulse transforms slow majority-spin d electrons (red) into fast sp electrons, thereby launching a spin current towards the AFM layer. The spin current crossing the interface results in the spin accumulation at the interface represented by spin chemical potential μ_s. (b) The typical time evolution of magnetization after femtosecond laser irradiation measured by TRMOKE experiment.

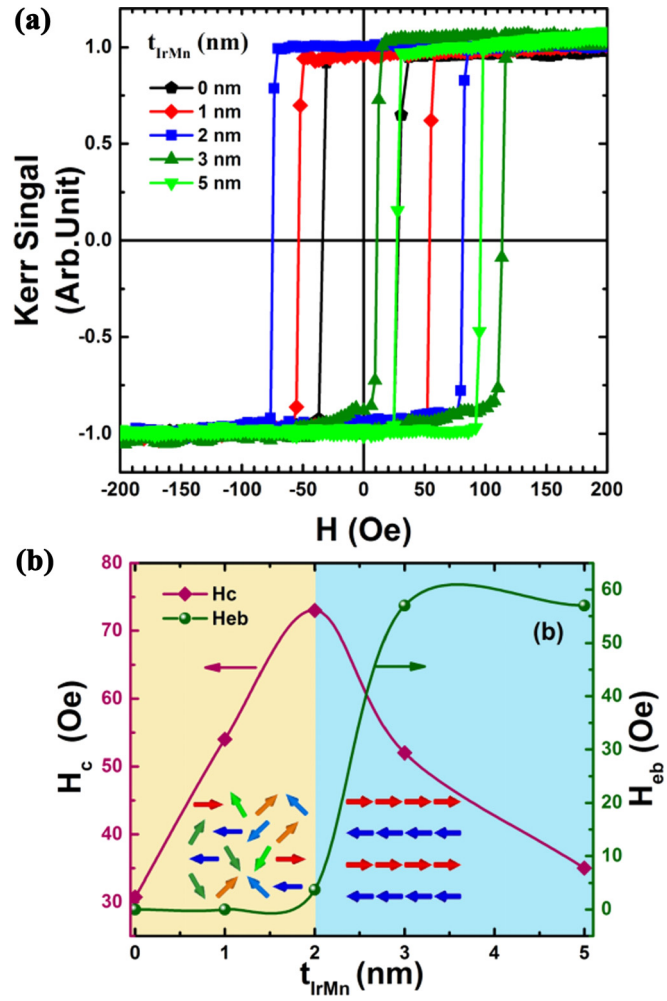

FIG. 2. Static magnetic properties of MgO/$Fe_{81}Ga_{19}$ (10 nm)/$Ir_{20}Mn_{80}$ (t nm) bilayers. (a) Longitudinal-MOKE loops with various thicknesses of IrMn layer t_{IrMn}. (b) Coercivity H_c and exchange bias field H_{eb} as a function of IrMn layer thickness t_{IrMn}.

II. RESULTS

A. Sample properties

$Ir_{20}Mn_{80}$ (t_{IrMn})/$Fe_{81}Ga_{19}$ (10-nm) bilayers [20] were deposited on optically transparent single-crystalline MgO (001) substrates in a magnetron sputtering system with a base pressure below 3×10^{-7} Torr. The substrates were annealed at 700 °C for 1 h in a vacuum chamber and then held at 250 °C during deposition. FeGa layers were obliquely deposited at an incidence angle of 45°. The IrMn layers were deposited while continuously rotating the substrates. In order to induce an exchange bias along the FeGa [010] direction, a magnetic field of 500 Oe provided by a permanent magnet was applied along the MgO [110] axis during growth. After deposition, a 3-nm protective Ta layer was deposited on the samples to avoid oxidation. The static longitudinal Kerr loops of $Fe_{81}Ga_{19}$ (10 nm)/$Ir_{20}Mn_{80}$ (t_{IrMn}) along FeGa [010] direction with various AFM IrMn thicknesses (t_{IrMn}) at room temperature were acquired using a laser diode with a wavelength of 650 nm.

Figure 2(a) shows the longitudinal Kerr loops of $Fe_{81}Ga_{19}$ (10 nm)/$Ir_{20}Mn_{80}$ (t_{IrMn}nm) along FeGa [010] direction with various AFM IrMn thicknesses (t_{IrMn}) at room temperature, whereas the thickness of the FM FeGa layer was fixed at 10 nm. For $t_{IrMn} \leqslant 2$ nm, the width of the hysteresis loops is enlarged with no obvious shift along the x axis, implying that the thickness of the IrMn layer is too thin to form an antiferromagnetic order for pinning the magnetization reversal of FeGa [21] [insert in Fig. 2(b) (left)]. For $t_{IrMn} > 2$ nm, the antiferromagnetic orders are well established, and consequently, the antiferromagnetic moments pin FM moments in reverse to induce a unidirectional anisotropy [insert in Fig. 2(b) (right)]. The loops therefore evidently exhibit exchange bias behavior. The exchange bias field achieves a value of about 60 Oe when $t_{IrMn} > 2$ nm, while the largest value of coercivity (~72 Oe) occurs at $t_{IrMn} = 2$ nm.

B. TRMOKE measurements for ultrafast demagnetization and Gilbert damping

We performed the polar TRMOKE experiment to measure ultrafast demagnetization time under a saturated applied field of 20 kOe in the normal direction of the samples [22]. The details of the TRMOKE experiment are described in Appendix A. Figure 3(a) shows the demagnetization curves for various IrMn thicknesses with a maximum magnetization

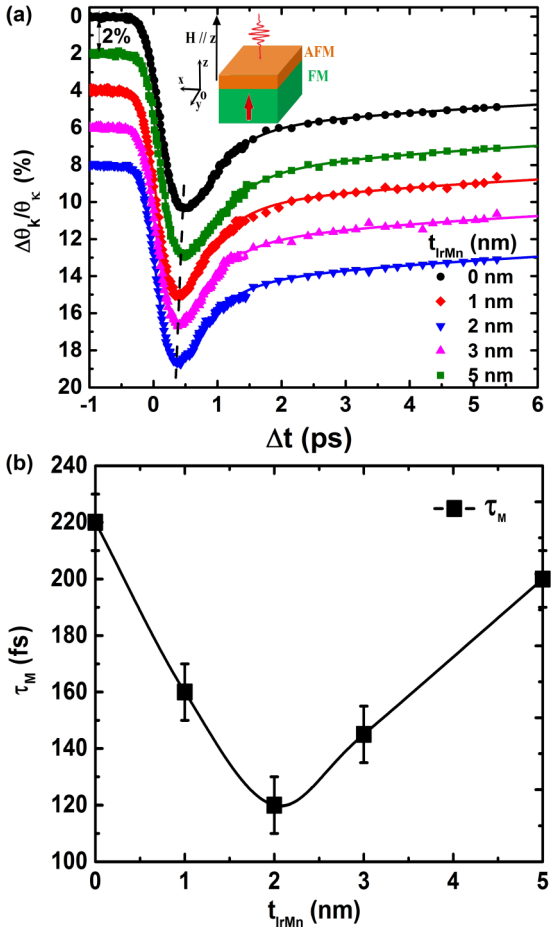

FIG. 3. Ultrafast demagnetization. (a) Ultrafast demagnetization curves with various IrMn layer thicknesses. The solid lines represent the fitting results by Eq. (1) in the text. The insert shows the configuration of the measurement for ultrafast demagnetization. (b) Ultrafast demagnetization time as a function of IrMn layer thickness.

quenching of ∼10% [23,24]. The temporal changes of the Kerr signals $\Delta\theta_k(t)$ were normalized by the saturation value θ_k just before the pump laser excitation. The time evolution of magnetization on subpicosecond timescales can be fitted according to Eq. (1) in terms of the three-temperature model (3TM) [17]:

$$-\frac{\Delta M(t)}{M} = \left\{\left[\left(\frac{A_1}{(t/\tau_0+1)^{0.5}} - \frac{A_2\tau_E - A_1\tau_M}{\tau_E-\tau_M}e^{-\frac{t}{\tau_M}} - \frac{\tau_E(A_1-A_2)}{\tau_E-\tau_M}e^{-\frac{t}{\tau_E}}\right)\Theta(t)\right]{}^{*}G(t,\tau_G)\right\}{}^{*}G(t,\tau_G), \quad (1)$$

where ${}^{*}G(t,\tau_G)$ represents the convolution product with the Gaussian laser pulse profile, τ_G is the FWHM of the laser pulses, τ_M is a step function, and τ_M is the Dirac δ function. A_1 represents the value of $\frac{\Delta M(t)}{M}$ after equilibrium between electrons, spins, and lattices. A_2 is proportional to the initial electron temperature rise. Here, we used the 780-nm laser as the pump pulse to excite the magnetic system out of equilibrium, while the 390-nm laser pulse was used as a probe beam. Therefore, in Eq. (1), the state filling effects during pump-probe experiment are neglected due to the different wavelengths of pump and probe beams used in this study. The cooling time by heat diffusion is described by τ_0, which should be about 1 order of magnitude larger than τ_E representing the timescale of electron-phonon interactions. The best-fitted value of $\tau_E = 500$ fs for all samples is in good agreement with that of previous reports [18]. The fitting parameters in Eq. (1) are shown in Table I, from which one notes the pulse width is 350 fs for all the samples. In our experimental setup, the time resolution is about 80 fs. In order to obtain a high time resolution, we measured the ultrafast demagnetization with a very fine step of time delay (15 fs). The values of ultrafast demagnetization time (120–220 fs) obtained from Eq. (1) are defined as the time needed for the magnetization to reach a level of e^{-1} of its maximum demagnetization. The time needed for magnetization to reach its maximum demagnetization (>500 fs) should be longer than the time extracted from Eq. (1). A similar result was reported by Vodungbo *et al.* [25]. The very large temporal stretching of the laser pulse up to 430 fs was attributed to the conversion of the incident laser pulse into a cascade of hot electrons. This could be one of the possible reasons resulting in the spread of laser pulse on the samples in this study. Via changing the single parameter τ_M we can accurately reproduce the experimental results for various samples. The ultrafast demagnetization time τ_M was observed to decrease from 220 ± 10 fs for $t_{IrMn} = 0$ nm to 120 ± 10 fs for $t_{IrMn} = 2$ nm, and then increase with further increasing t_{IrMn} [Fig. 3(b)].

TABLE I. Values of the main fit parameters of ultrafast demagnetizations curves for various thicknesses of the samples.

t_{IrMn} (nm)	τ_M(fs)	τ_E(fs)	τ_0(ps)	τ_G(fs)	A1	A2
0	220 ± 10	500	5	350	0.8	2
1	160 ± 10	500	6	350	0.8	2
2	120 ± 10	500	7	350	0.8	2
3	145 ± 10	500	4	350	0.8	2
5	200 ± 10	500	5	350	0.8	2

The precessional frequency and damping factor can be derived by means of the TRMOKE signals as well [26,27]. Figure 4(a) shows the typical time evolution of the polar component of magnetization after pump laser excitation at different fields applied along the [110] direction of FeGa for $t_{IrMn} = 2$ nm. It is observed clearly that the spin precession process can obviously be influenced by applied fields. The exact values for f with various applied fields can be obtained using the damped harmonic function added to an exponential-decaying background:

$$\Delta M(t) = A + B\exp(-vt) + C\exp\left(-\frac{t}{\tau}\right)\sin(2\pi ft + \varphi), \quad (2)$$

where A and B are the background magnitudes, and v is the background recovery rate. C, τ, f, and φ are the magnetization precession amplitude, relaxation time, frequency, and phase, respectively. The field dependence of frequency f extracted from the fitting procedure is shown in Fig. 4(b). We note that the experimental f-H relation can be reproduced very

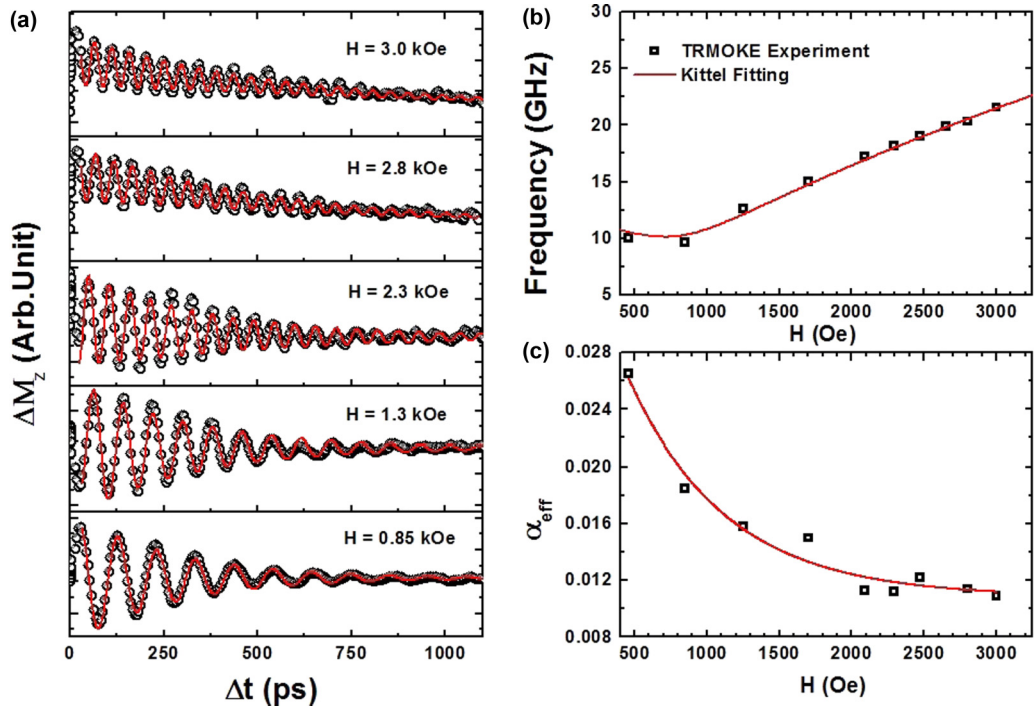

FIG. 4. Spin precession. (a) TRMOKE signals of FeGa/IrMn bilayers with $t_{\mathrm{IrMn}} = 2$ nm in various applied fields. (b) Precessional frequency as a function of applied fields. (c) Effective Gilbert damping constant as a function of applied fields.

well by the Kittel equation (3) [27]:

$$\left(\frac{2\pi f}{\gamma}\right)^2 = \frac{1}{M_s^2} H_1 H_2, \tag{3}$$

with $H_1 = -2K_{\mathrm{out}} + 4\pi M_s^2 + 2K_u \cos^2\varphi_M + 2K_1 - K_1 \sin^2 2\varphi_M + HM_s \cos(\varphi_M - \varphi_H) + K_{eb} \cos\varphi_M$ and

$$H_2 = 2K_1 \cos 4\varphi_M + 2K_u \cos 2\varphi_M + M_s H \cos(\varphi_M - \varphi_H) + K_{eb} \cos\varphi_M.$$

And $\gamma = \gamma_e g/2$ is the gyromagnetic ratio. φ_M and φ_H are the angles of in-plane equilibrium M and H with respect to the FeGa [010] easy axis. K_1, K_u, K_{eb}, and K_{Out} are the in-plane magnetocrystalline, uniaxial, unidirectional, and out-of-plane magnetic anisotropy constants of FeGa films, respectively. The value of the magnetocrystalline anisotropy constant is $K_1 = 4.5 \times 10^5$ erg/cm^3 for the samples with various AFM layer thicknesses during the fitting procedure and the uniaxial magnetic anisotropy constant $K_u = (1.5 \pm 0.3) \times 10^5$ erg/cm^3. For $t_{\mathrm{IrMn}} = 3$ and 5 nm, the unidirectional magnetic anisotropy constant of $K_{eb} = 3 \times 10^4$ erg/cm^3 has to be included for more accurate fitting, although it is 1 order of magnitude smaller than those of magnetocrystalline and uniaxial anisotropy.

The effective Gilbert damping factor α_{eff} shown in Fig. 4(c) is determined from the relaxation time τ by Eq. (4) [28]:

$$\alpha_{\mathrm{eff}} = 2/\tau\gamma(H_1 + H_2). \tag{4}$$

Since the overall effective damping factor α_{eff} consists of intrinsic damping and extrinsic damping, whereby the second one arises from both the two-magnon-scattering and the dephasing effect in the samples, the overall effective Gilbert damping factor decreases monotonously to a constant value with increasing the applied field [Fig. 4(c)]. As one of the mainly extrinsic contributions, the two-magnon-scattering induced damping has been extensively studied in exchange-biased heterostructures [29–34]. The mature theory was developed to explain the two-magnon scattering process due to spatial fluctuations of anisotropy and exchange bias field [30,35]. The two-magnon scattering process comes from the scatterings of the uniform ($k = 0$) precession mode into nonuniform modes ($k \neq 0$ magnons) that are degenerate in frequency. This process is described by the Hamiltonian, in which the spatial fluctuation in the exchange coupling caused by interface roughness determines the scattering strength. The roughness gives rise to a large fluctuating field because the FM magnetization interacts alternatively with one or the other AF sublattice via the atomic exchange coupling. It is a well-known relaxation mechanism effective in exchange-biased heterostructures due to the interface roughness occurring on the short length scales. When a low external field comparable with the exchange bias field was applied, the two-magnon scattering effect resulted in the increase of Gilbert damping with the exchange bias field according to previous reports [33,34]. However, as shown in Ref. [36], a strong enough applied field can be used to exclude the contributions from the two-magnon scattering, where the value of Gilbert damping factor keeps as a constant with various two-magnon-scattering strength. Based on this result, a similar method using strong enough external fields was applied in this study to exclude the two-magnon-scattering effect. Moreover, previous works show that the two-magnon-scattering induced damping increases with precession frequency because of the increased degeneracy of spin waves [37,38]. Our work demonstrated that the damping factor keeps almost a constant value at high enough applied fields, indicating the minor contributions from

the two-magnon-scattering to Gilbert damping. Besides, it has been demonstrated previously that the two-magnon-scattering contributions decrease monotonously with increasing the film thickness [33,34]. This again disagrees with the tendency of thickness dependence of damping at high applied field shown in Fig. 5(c). Therefore, in this study, the two-magnon-scattering strength was suppressed effectively by applying a high enough external field. On the other hand, inhomogeneities in FeGa thin film may cause variations in the local magnetic anisotropy field, which leads to the variations of spin orientations when the external field is not large enough and gives rise to the enhanced damping arising from the spin dephasing effect [28]. However, an applied field (∼kOe) much larger than the anisotropy field makes the spin orientation uniform; as a result, the dephasing effect is suppressed largely. Based on the above analysis, the intrinsic part of damping is independent of the external field or precession frequency, while the extrinsic part including both the dephasing effect and the two-magnon-scattering effect are field dependent. In order to avoid the effect of the extrinsic damping factor, the intrinsic damping factors were obtained by fitting the overall damping factor as a function of applied fields with Eq. (5) [39,40], shown as the red line in Fig. 4(c):

$$\alpha_{\text{eff}} = \alpha + \alpha_1 e^{-H/H_0}, \tag{5}$$

where α and $\alpha_1 e^{-H/H_0}$ are the intrinsic and extrinsic parts of the damping factor, respectively.

For the derivation of spin precessional frequency as well as the Gilbert damping, the similar producers as shown above were adapted to various samples. Figure 5(a) shows the precessional frequency from oscillation curves with various IrMn thicknesses. Since the exchange bias field and coercivity are much weaker than the applied fields, the f-H curves of FeGa films are therefore slightly different with various AFM layer thicknesses, which is in contrast to the observation that the enhanced uniaxial anisotropy of Fe/CoO bilayers [28] greatly increases the precessional frequency. More importantly, we find the effective damping factor α_{eff} decreases with applied fields [Fig. 5(b)]. The solid lines represent the fitting expression shown as Eq. (5). Interestingly, the effective Gilbert damping factors drop to as nearly a constant value as the intrinsic damping factor when the applied fields increase enough to suppress the extrinsic contributions as stated above.

The values of the intrinsic damping factor as a function of the thickness of the IrMn layer are illustrated in Fig. 5(c). It increases first and reaches the maximum value with the thickness of the IrMn layer at $t_{\text{IrMn}} = 2$ nm and finally decreases with further increasing the thickness of the IrMn AFM layer. A drastic change of 2.5 times for damping occurs at $t_{\text{IrMn}} =$ 2 nm. Similarly, Azzawi *et al.* showed around 2 times enhancement of damping in NiFe/Pt bilayers when a continuous Pt capping layer is just forming at 0.6 nm by TRMOKE measurements [41]. Moreover, once a continuous IrMn layer is forming at 2 nm, the accompanied strong intrinsic anisotropy of AFM would contribute partly to the damping enhancement superimposed to the spin pumping effect. This has been demonstrated previously by Zhang *et al.*, where the damping of Py/IrMn bilayers is 3 or 4 times larger than that in the Py/Cu/IrMn samples [42]. Based on the discussions in Fig. 4, we can exclude the extrinsic mechanisms such as the two-magnon-scattering and the dephasing effect as the dominant contributions to the damping process when the external fields are high enough [43]. Besides, FeGa alloys are

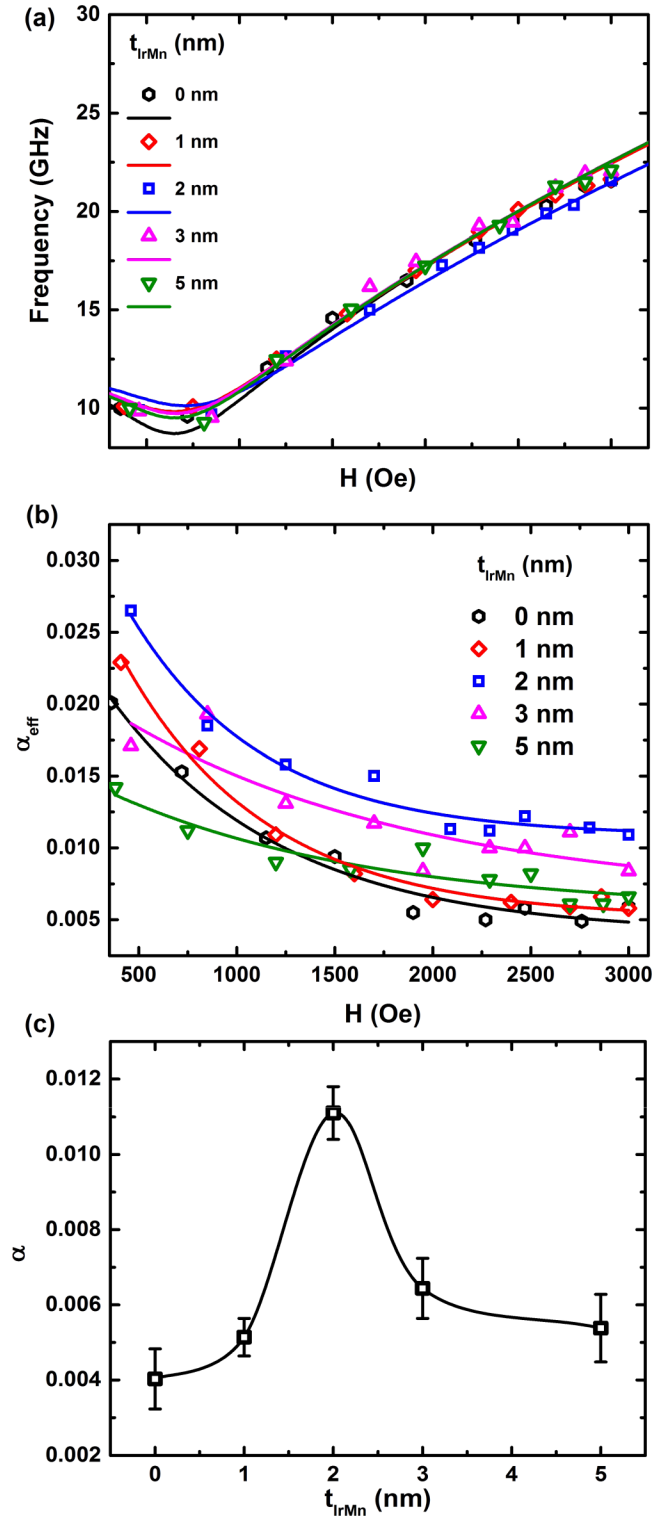

FIG. 5. Frequency and damping of spin precession. (a) Frequency of spin precession as a function of applied fields with various IrMn thicknesses. The solid lines represent the fitting results by Kittle equations. (b) Effective Gilbert damping constants as a function of applied fields with various IrMn thicknesses. (c) Intrinsic Gilbert damping as a function of IrMn thickness.

particularly interesting because of their magnetoelastic properties [44]. The acoustic waves possibly are triggered by ultrashort laser, and as a result, spin precession would be excited nonthermally via a magnetoelastic effect [45]. However, this effect can be excluded based on the following reasons: first, the external field has to be applied along with the hard axis of FeGa; otherwise, the magnetization precession cannot be induced. It agrees with the fact that the canted magnetization from the easy axis is necessary when the spin precession arising from instantaneous anisotropy change accompanied by ultrafast demagnetization occurs [26]. In contrast, the occurrence of spin precession from the magnetoelastic effect is independent of initial magnetization orientation. Second, in order to check the contribution of the resonance mode from the magnetoelastic effect, we performed a fast Fourier transform in Appendix B. Only the uniform field-dependent precession mode was excited at the present study. This is not the expected behavior for the acoustically induced modulation of the magneto-optical effects. Therefore, the magnetoelastic effect of FeGa was largely suppressed in this study. This is probably because the laser fluence of around $1\,\mathrm{mJ/cm^2}$ is not high enough to induce a large amplitude of strain pulse. According to Ref. [45], the oscillation amplitude of the acoustic mode increases linearly with the laser energy density within the probed range. Moreover, the FeGa material with a thickness as thick as 60 nm is preferred to induce an obvious magnetoelastic behavior [46], while 10 nm at the present experiment is probably too thin. As a result, the intrinsic damping can be influenced by the following parameters: (1) the magnetocrystalline anisotropy of FM [47], (2) the exchange bias field [30,31,36], and (3) the spin pumping effect at the interface between FM and AFM [15,16,42,48]. In the case of FeGa/IrMn bilayers, the magnetocrystalline anisotropy constant of FeGa $K_1 = 4.5 \times 10^5\,\mathrm{erg/cm^3}$ obtained from Figs. 4 and 5 is invariant with the AFM layer thickness. Moreover, referring to Fig. 2(b), it seems that there is no direct relationship between the intrinsic damping factor and the exchange bias field H_{eb}. When the applied field is far higher than the exchange bias field, both the precessional frequency and the damping factor show independence of exchange bias field [36]. Therefore, the IrMn thickness dependence of the intrinsic damping is not attributed to the magnetocrystalline anisotropy and the exchange bias field. Due to the strong spin-orbit coupling of the heavy metal (HM) Ir in the IrMn alloy, the contribution of spin pumping to the damping factor must be taken into account. It is noteworthy that the IrMn thickness dependence of damping in FeGa/IrMn is different from that in other normal FM/HM bilayers, where the damping factor increases monotonically with the thickness of the HM layer and approaches a saturation value [49]. However, the damping of the FeGa ferromagnetic layer decreases again after reaching a peak value at $t_{\mathrm{IrMn}} = 2$ nm. The change of the damping factor is always accompanied by the spin current transfer between FM and AFM layers. More spin currents absorbed by the neighboring layer result in larger damping in the FM layer. An unconventional decrease of the damping factor implies that not only does the effect of heavy metal Ir in IrMn alloy have to be taken into account but also the antiferromagnetic magnetization. The heavy metal Ir serves as a perfect spin sink to absorb the spin currents and consequently increases the damping in FeGa, while the antiferromagnetic magnetization in IrMn serves as a new source to compensate for the dissipation of magnetization precession and decreases the damping of FeGa.

C. First-principles calculations for IrMn layer thickness dependence of Gilbert damping

To understand the behavior of the IrMn thickness-dependent damping factor, we calculated the damping factor using the scattering theory of magnetization dissipation combined with the first-principles electronic structure [50]. The calculated FM/AFM bilayer structure shown in Fig. 6(a) is the same as that in the experiment. Here, the magnetic moments of AFM sublattices serve as not only a spin sink to absorb the spin current pumped from the adjacent FM layer but also a spin current emitter to partly cancel the spin pumping effect of the FM. The interfacial exchange coupling forces the magnetic moments of the IrMn sublattices in a few layers near the interface to precess following the adjacent FM, generating spin currents back into the FM layer [Fig. 6(b)]. Based on this model, the enhancement of damping due to the spin current $\alpha_{sp} = \Delta\alpha = \alpha_{t_{\mathrm{IrMn}}} - \alpha_{t_{\mathrm{IrMn}}=0\ \mathrm{nm}}$ as a function of IrMn thickness was calculated and shown as the solid circle in Fig. 6(c). It increases first to a peak value at $t_{\mathrm{IrMn}} = 2$ nm and then drops with further increasing the IrMn layer thickness. When $t_{\mathrm{IrMn}} \leqslant 2$ nm, the thickness of the IrMn layer is too thin to establish the antiferromagnetic order, which can be supported by the negligible exchange bias as shown in Fig. 2(b). In this case, the pumped spin current from the AFM back into the FM to partially cancel the spin pumping effect by the FM is largely reduced because of the disorder of the antiferromagnetic moments, as illustrated on the left side in Fig. 6(b). In this region, therefore, the magnetic moments in the AFM serve as a perfect spin sink to absorb the spin current pumped from the adjacent FM, resulting in a significant enhancement in the damping factor. For the samples with the thickness of IrMn $t_{\mathrm{IrMn}} > 2$ nm, however, the antiferromagnetic order is well established and the accompanied exchange bias is remarkably large [see Fig. 2(b) and its insert]. Because of the exchange coupling between FM and AFM at the interface, the magnetic moments of the AFM sublattices in a few layers near the interface are forced to precess following the magnetic moment of the FM, while those far away from the interface would stay static. Such an exchange spring effect at the interface caused spin precession in the AFM layer, and consequently, spin currents would be transferred from AFM to the FM layer. Moreover, these spin currents from the AFM would be enhanced due to the coherent precession of magnetization in different sublattices, as illustrated in the right side of Fig. 6(b). The exchange spring-effect-induced precession of the AFM has two effects: (1) the AFM has intrinsic damping that increases the overall damping of the FM/AFM bilayer, and (2) the precessional motion of magnetic moments in AFM sublattices pumps spin currents into the FM, which partly cancels the spin pumping by the FM. As a result, the overall damping of the bilayers is reduced. From the solid circles in Fig. 6(c), one can see that the damping decreases with increasing t_{IrMn} when $t_{\mathrm{IrMn}} > 2$ nm, indicating that the latter effect of the pumped spin currents is dominant over the

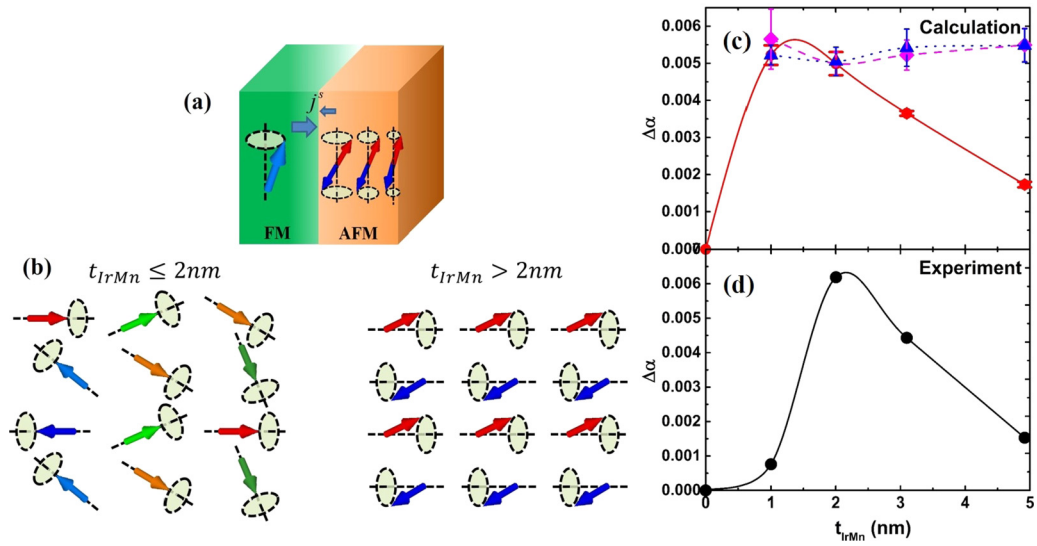

FIG. 6. Results of first-principles calculations. (a) Illustration of the ferromagnet (FM)/antiferromagnet (AFM) structure employed to investigate the spin transport. (b) The configuration of the IrMn magnetic moments located at the first layer near the interface. (c) The calculated damping enhancement as a function of the thickness of the antiferromagnetic IrMn. The solid circles show the calculated damping enhancement with the precession of AFM magnetic moments. The solid diamonds show the calculated damping enhancement with perfectly static AFM ordered IrMn without precession, while the solid triangles correspond to the calculated values using a static paramagnetic IrMn layer with vanishing Néel order. (d) The experimental damping enhancement as a function of the thickness of antiferromagnetic IrMn.

intrinsic damping. Besides, by comparing the calculated and experimental values [Figs. 6(c) and 6(d)], one can find that the calculated Gilbert damping is larger than the experimental one for $t_{\mathrm{IrMn}} = 1$ nm. The reason for the deviation is the assumption of a perfectly flat FeGa/IrMn interface in the calculation, which leads to a larger spin current pumped from the FM. Unfortunately, it is almost impossible to fabricate the perfectly flat film when the thickness is less than 1 nm.

In order to separate the contribution of the precession of the magnetic moment of the AFM sublattice to damping, we also calculated the damping by assuming perfectly static AFM ordered IrMn without precession [solid diamonds in Fig. 6(c)] and a paramagnetic IrMn layer with vanishing Néel order [solid triangles in Fig. 6(c)]. The calculated results demonstrate that if the magnetic moments of the AFM sublattice either do not precess or align randomly, the IrMn layers serve only as a perfect spin sink to absorb the spin currents pumped from the adjacent FM, resulting in a significant enhancement of damping. The damping increases monotonically to a saturation value with IrMn thickness, which is similar to that of heavy metals [49].

D. Relationship between ultrafast demagnetization rate and Gilbert damping induced by nonlocal spin currents

The central strategy of our study is to establish a direct correlation between τ_M and α. According to Figs. 3(b) and 5(c), we find that the femtosecond laser-induced ultrafast demagnetization time τ_M and the Gilbert damping α show an opposite IrMn thickness dependence in FeGa/IrMn bilayers. By plotting τ_M versus α as shown in Fig. 7(a), one can clearly observe that the value of τ_M decreases with α, suggesting that spin transport acts as an additional dissipation channel for accelerating the ultrafast demagnetization and enhancing the damping. The damping factor $\alpha_{t_{\mathrm{IrMn}}}$ for $t_{\mathrm{IrMn}} > 0$ nm is ascribed to the spin pumping effect induced by various AFM thicknesses α_{sp} and the contribution from the FM itself, $\alpha_{t_{\mathrm{IrMn}}=0\ \mathrm{nm}}$.To give further insight into the relationship, we replotted Fig. 7(a) by using the change of the ultrafast demagnetization rate $\Delta\frac{1}{\tau_M} = \frac{1}{\tau_M}|_{t_{\mathrm{IrMn}}} - \frac{1}{\tau_M}|_{t_{\mathrm{IrMn}}=0\ \mathrm{nm}}$ versus the enhancement of Gilbert damping $\alpha_{sp} = \Delta\alpha = \alpha_{t_{\mathrm{IrMn}}} - \alpha_{t_{\mathrm{IrMn}}=0\ \mathrm{nm}}$ induced by the spin current. An approximately linear relationship is confirmed and shown in Fig. 7(b), which can be fitted using Eq. (6):

$$\Delta\frac{1}{\tau_M} = \frac{\mu_s}{\hbar}\Delta\alpha, \tag{6}$$

where $\Delta\frac{1}{\tau_M}$, $\Delta\alpha$ represents the enhancement of ultrafast demagnetization rate and Gilbert damping induced by the spin current, respectively, μ_s is the spin chemical potential, and $\hbar$ is the Planck constant. (For the derivation of Eq. (6), please see Appendix D for details). A reasonable value of $\mu_s \approx 1$ eV, which is similar to that of spin splitting in $3d$ transition metals, was obtained by the linear fitting using Eq. (6).

The spin chemical potential μ_s is proportional to spin accumulations at the interface between different layers. It contributes largely to ultrafast demagnetization according to the model of laser-induced ultrafast superdiffusive spin transport in layered heterostructures [14,51]. There is a large difference in velocities or lifetimes for spin-dependent hot electrons [52]. As a result, the transport properties of hot electrons are spin dependent. For instance, the minority-spin electrons excited by an ultrashort laser survive for only a very short time, and they decay to nonmobile bands approximately at the position they were excited. Instead, majority-spin electrons have longer lifetimes and higher velocities, so they leave fast from the excitation region after being created, in part a result of the demagnetization process. Because the directions

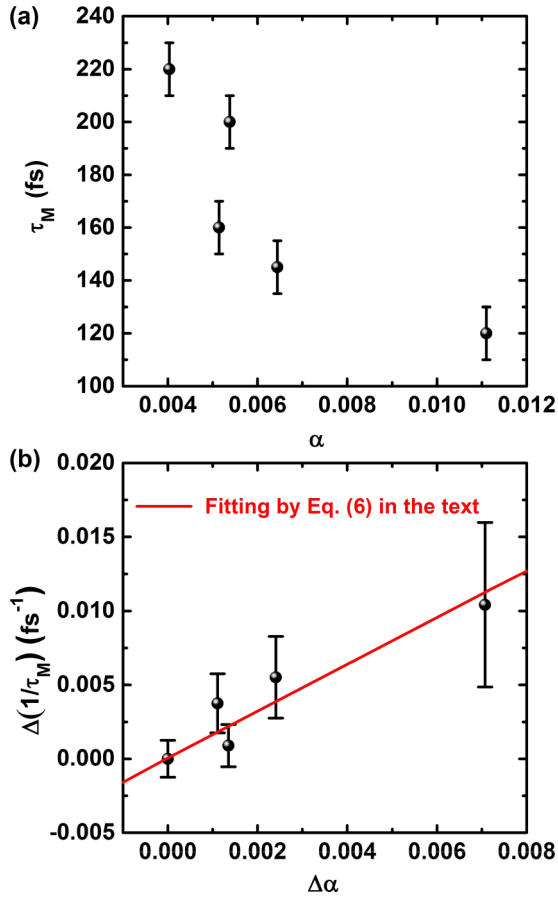

FIG. 7. (a) Ultrafast demagnetization time as a function of Gilbert damping. (b) The variation of ultrafast demagnetization rate as a function of Gilbert damping enhancement. The red line indicates the fitting via Eq. (6) in the text.

of motion for all the electrons are random, they can obtain a velocity directed back towards the ferromagnetic film. A second part of the demagnetization is ascribed to the backflow of spin-minority electrons from the substrate or the neighboring layer. Spin-majority electrons entering the ferromagnetic layer will find good transport properties and continue diffusing without severely decaying. However, spin-minority electrons experience a considerable worsening of the transport properties as soon as they enter the ferromagnetic layer. The consequence is that they are trapped at the entrance of the ferromagnetic layer, giving rise to the spin accumulations at the interface. Nevertheless, the quantitative description for spin accumulations during ultrashort laser-induced demagnetization in heterostructures is still lacking. This work aims at filling this gap by relating ultrafast demagnetization time and Gilbert damping. A detailed calculation for the value of 1 eV for spin chemical potential obtained in this experiment is highly desirable.

The nonlocal spin currents dissipated at the interface of FeGa/IrMn open an additional channel to accelerate the ultrafast demagnetization and enhance the Gilbert damping. However, in the case of the sample with $t_{\mathrm{IrMn}} = 0$ nm without the assistant AFM layer, both the local spin-flip and nonlocal spin transport mechanisms probably contribute to the ultrafast demagnetization in the ferromagnetic layer. For instance, based on the breathing Fermi-surface model of the Gilbert damping and the Elliott-Yafet relation for the spin-relaxation time, a relation shown as Eq. (7) is established between the conductivitylike Gilbert damping α and ultrafast demagnetization time τ_M [10]:

$$\tau_M = \frac{M}{\gamma F_{el} p b^2}\alpha. \tag{7}$$

Taking the values of $\tau_M|_{t_{\mathrm{IrMn}}=0\ \mathrm{nm}}$ and $\alpha|_{t_{\mathrm{IrMn}}=0\ \mathrm{nm}}$ as 220 fs and 0.004, respectively, a value of $\alpha/\tau_M = 1.8 \times 10^{10}\ \mathrm{s}^{-1}$ is derived. This value is reasonable and agrees well with that of $3d$ transition metal Ni calculated by the breathing Fermi-surface model [53], indicating that the ultrafast demagnetization of ferromagnetic FeGa film itself is mainly governed by the local spin-flip scattering events. Nonetheless, we note that ultrafast demagnetization in the ferromagnetic layer was accelerated and the Gilbert damping was enhanced via the interfacial spin accumulations once the IrMn layer was attached.

III. CONCLUSIONS

The unconventional IrMn thickness dependence of α is attributed to the cancellation of the spin currents pumped from the AFM IrMn layer to the FM FeGa layer. We establish a proportional relationship between the change of ultrafast demagnetization rate and the enhancement of Gilbert damping induced by the spin currents via the interfacial spin chemical potential. This result can facilitate the utilization of ultrafast spintronic devices in the terahertz region.

ACKNOWLEDGMENTS

This work is supported by the National Key Research Program of China (Grants No. 2015CB921403, No. 2016YFA0300701, and No. 2017YFB0702702), the National Natural Sciences Foundation of China (Grants No. 91622126, No. 51427801, and No. 51671212), and the Key Research Program of Frontier Sciences, CAS (Grants No. QYZDJ-SSW-JSC023, No. KJZD-SW-M01, and No. ZDYZ2012-2). The work at Beijing Normal University is partly supported by the National Natural Sciences Foundation of China (Grants No. 61774017, No. 61704018, and No. 11734004), the Recruitment Program of Global Youth Experts, and the Fundamental Research Funds for the Central Universities (Grant No. 2018EYT03). The work at East China Normal University is partly supported by the National Natural Sciences Foundation of China (Grant No. 11874150).

APPENDIX A: TIME-RESOLVED MAGNETO-OPTICAL KERR EFFECT MEASUREMENTS

In this study, the dynamical process of fast and ultrafast spin dynamics was measured by time-resolved magneto-optical Kerr effect (TRMOKE) measurements. The experiments were carried out using an all-optical pump-probe technique. A train of optical pulses with a wavelength of 780 nm, 55-fs duration, and 100 nJ/pulse is generated at 5.2 MHz repetition rate by a Ti:sapphire oscillator (Femtolaser, XL-100). A 200-μm thickness beta barium borate (BBO) crystal

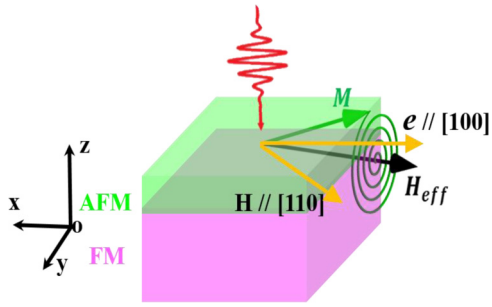

FIG. 8. Scheme of TRMOKE experiment for spin precession dynamics.

was used to double the frequency of the femtosecond laser. The laser beam from the source is split into both 780- and 390-nm beams. We use the 780-nm laser as the pump pulse to excite the magnetic system out of equilibrium, while the 390-nm laser pulse was used as a probe beam to measure the subsequent magnetization dynamics with the timescale from subpicosecond to nanosecond. The pump laser beam is much stronger than the probe, with an intensity ratio of about 100 for all the measurements. Both the pump and probe beams are incident along the normal axis (z axis) of the samples. The detection geometry is only sensitive to the out-of-plane component of the magnetization M_z. For fast spin dynamics, we applied various external fields along the $Fe_{81}Ga_{19}$ [110] direction to trigger the spin precession, while a large enough field of about 20 kOe was applied along the $Fe_{81}Ga_{19}$ [001] direction to obtain the ultrafast demagnetization curves. We adjusted the pump laser fluence from 1 to 1.25 mJ/cm^2 to obtain the same maximum quenching for various samples. The pump and probe beams are focused onto the samples with spot diameters of ~10 and ~5 μm, respectively, via an objective lens. For the spin precession measurements, the scheme of the TRMOKE experiment is illustrated in Fig. 8. The signals are sensitive to the polar component of magnetization after pump laser excitation at different fields applied along the [110] direction of FeGa.

APPENDIX B: FAST FOURIER TRANSFORM ANALYSIS

The ferromagnetic FeGa is a famous material for its magnetoelastic properties. After femtosecond laser irradiation, an external field-independent resonance mode is triggered due to the excitation of coherent acoustic phonons. However, only one field-dependent resonance mode was excited in this study according to fast Fourier transform analysis in Fig. 9.

APPENDIX C: FIRST-PRINCIPLES CALCULATIONS

The electronic structure of the FeGa/IrMn bilayer is calculated self-consistently using the local density approximation of the density functional theory. The spin-dependent potentials, charge and spin densities are obtained with the minimal basis of tight-binding linear muffin-tin orbitals. In the calculation of the total damping, the scattering region, consisting of the repeated FeGa/IrMn bilayers, is connected to two semi-infinite Cu leads. We have introduced the thermal lattice disorder into a 4 × 4 supercell and displaced the atoms

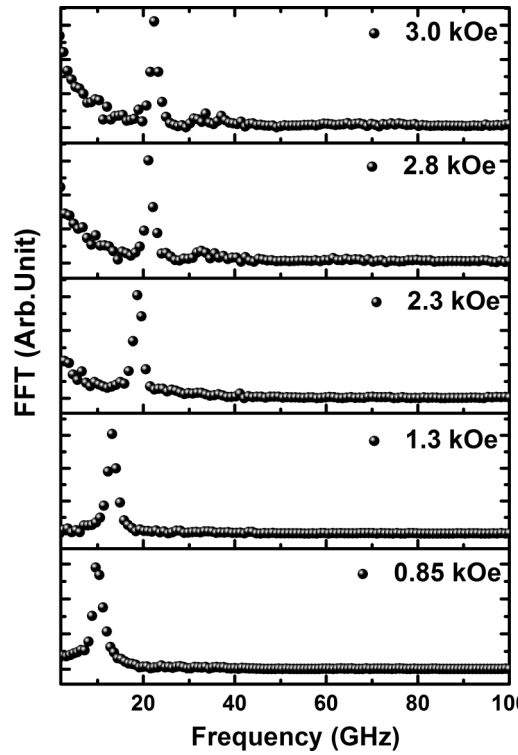

FIG. 9. Fourier transform spectra measured between 0.85 and 3.0 kOe for $t_{IrMn} = 2$ nm.

in the scattering region randomly away from their equilibrium positions with a Gaussian distribution. The root-mean-square atomic displacements of the Gaussian distribution are determined using a simple Debye model with a Debye temperature of 470 K. The two-dimensional Brillouin zone of the supercell is sampled by a 24 × 24 k mesh corresponding to the 96 × 96 mesh for the Brillouin zone for the 1 × 1 unit cell. The effect of magnons in the FM FeGa is neglected in our calculation. This is because the magnetic damping is dominated by electrons at the Fermi level in metals, which can efficiently transfer spin angular momentum into the orbital motion via spin-orbit interaction. In metals and alloys, the influence of magnon-phonon coupling is negligible, except for near the Curie temperature [54].

If magnetization precession occurs only in the FM FeGa layer, the calculated damping enhancement does not sensitively depend on the specific order of the AFM IrMn. Here we take two limits: the perfectly antiferromagnetic ordered IrMn and the paramagnetic IrMn. (The magnetic moments of Mn are randomly distributed such that both the Néel order and total magnetization vanish). The damping enhancements calculated for the two cases are nearly identical, where the damping factor is enhanced and saturates at a thickness of 2 nm. It indicates that the pumped spin current by the precessional FeGa is immediately absorbed by the IrMn layer. The large moment on the Mn atom can absorb the pumped transverse spin current efficiently. On the other hand, the AFM IrMn is forced to precess due to the interfacial exchange coupling; however, the efficiency of the spin current generation by AFM depends on its specific order. It is suppressed largely in the case of paramagnetic IrMn because of the

cancellation via magnetic moments with various orientations shown on the left side of Fig. 6(b) in the main text. In contrast, the efficiency of the spin current generation by the AFM is enhanced remarkably by the coherent precession of the ordered magnetic moments shown in the right side of Fig. 6(b) in the main text. The cone angle of precessional IrMn is modeled to exponentially decay from the interface with a typical decay length of 2 nm. The precessional AFM has mainly two contributions to the damping enhancement of the bilayer. First, the AFM has intrinsic damping that increases the total energy loss during the magnetization dynamics. The second effect is that the precessional AFM pumps spin current into the FM that cancels partly the spin pumping by the FM and decreases the damping enhancement.

APPENDIX D: DERIVATION OF EQ. (6) IN THE MAIN TEXT

It is well known that the magnetic moment $\vec{M}_s$ is proportional to the spin angular momentum $\vec{S}$ via gyromagnetic ratio $\gamma = \frac{g\mu_B}{\hbar}$,

$$\vec{M}_s = \gamma \vec{S}, \tag{D1}$$

where g is the Landé factor and μ_B is the Bohr magneton. Normally, we take $\vec{M} = V\vec{M}_s$ as the total magnetic moments, where V is the volume of the atom.

τ_M is the ultrafast demagnetization time. Therefore, the value of $\frac{1}{\tau_M}$ is taken as the demagnetization rate. The demagnetization is always accompanied by dissipation of the spin angular momentum, and hence the rate of spin angular momentum dissipation is

$$\frac{\vec{m}}{\gamma} \cdot \frac{1}{\tau_M}. \tag{D2}$$

On the other hand, the spin current $\overrightarrow{j^s}$ per unit area generated by spin pumping effect reads

$$\overrightarrow{j^s} = \frac{1}{4\pi} g_{\text{eff}} \overrightarrow{\mu_s}, \tag{D3}$$

where g_{eff} is the effective interfacial spin-mixing conductance including the influence of the backflow spin current from the AFM IrMn to FeGa, and $\vec{\mu}_s$ is the spin-accumulation-driven chemical potential. The pumped spin current across the interface is $\overrightarrow{I^s} = \overrightarrow{j^s} A$, where A is the area of the interface:

$$g_{\text{eff}} = \frac{4\pi M_s d\, \Delta\alpha}{g\mu_B}, \tag{D4}$$

where d is the thickness of the ferromagnetic layer, $\Delta\alpha = \alpha_{t_{\text{IrMn}}} - \alpha_{t_{\text{IrMn}}} = 0$ nm is the enhancement of Gilbert damping induced by the absorption and generation of spin current via various IrMn thicknesses.

Therefore, if we correlate the spin angular momentum dissipated by the ultrafast demagnetization and that induced by spin pumping, the relationship reads

$$\frac{\vec{m}}{\gamma} \cdot \frac{1}{\tau_M} = \vec{I}^s. \tag{D5}$$

Then we take Eq. (10) into Eq. (12), and we can correlate the parameters τ_M and α via

$$\frac{1}{\tau_M} = \frac{\mu_s}{\hbar} \Delta\alpha. \tag{D6}$$

To exclude the contributions from local spin-flip scattering mechanisms to the ultrafast demagnetization rate represented by $\frac{1}{\tau_M}|_{t_{\text{IrMn}}} = 0$ nm, the value of $\frac{1}{\tau_M}$ is replaced by $\Delta\frac{1}{\tau_M} = \frac{1}{\tau_M}|_{t_{\text{IrMn}}} - \frac{1}{\tau_M}|_{t_{\text{IrMn}}} = 0$ nm.

[1] T. Seifert, S. Jaiswal, U. Martens, J. Hannegan, L. Braun, P. Maldonado, F. Freimuth, A. Kronenberg, J. Henrizi, and I. Radu, Nat. Photonics. **10**, 483 (2016).

[2] E. Beaurepaire, J. C. Merle, A. Daunois, and J. Y. Bigot, Phys. Rev. Lett. **76**, 4250 (1996).

[3] B. Koopmans, J. J. M. Ruigrok, F. Dalla Longa, and W. J. M. de Jonge, Phys. Rev. Lett. **95**, 267207 (2005).

[4] U. Atxitia and O. Chubykalo-Fesenko, Phys. Rev. B **84**, 144414 (2011).

[5] U. Atxitia, O. Chubykalo-Fesenko, J. Walowski, A. Mann, and M. Münzenberg, Phys. Rev. B **81**, 174401 (2010).

[6] B. Koopmans, G. Malinowski, F. Dalla Longa, D. Steiauf, M. Fähnle, T. Roth, M. Cinchetti, and M. Aeschlimann, Nat. Mater. **9**, 259 (2009).

[7] J. Walowski and M. Münzenberg, J. Appl. Phys. **120**, 140901 (2016).

[8] J. Walowski, G. Muller, M. Djordjevic, M. Münzenberg, M. Klaui, C. A. F. Vaz, and J. A. C. Bland, Phys. Rev. Lett. **101**, 237401 (2008).

[9] I. Radu, G. Woltersdorf, M. Kiessling, A. Melnikov, U. Bovensiepen, J.-U. Thiele, and C. H. Back, Phys. Rev. Lett. **102**, 117201 (2009).

[10] W. Zhang, W. He, X. Q. Zhang, Z. H. Cheng, J. Teng, and M. Fähnle, Phys. Rev. B **96**, 220415(R) (2017).

[11] Y. Ren, Y. L. Zuo, M. S. Si, Z. Z. Zhang, Q. Y. Jin, and S. M. Zhou, IEEE Trans. Magn. **49**, 3159 (2013).

[12] Z. Zhang, D. Wu, Z. Z. Luan, H. C. Yuan, Z. Z. Zhang, J. H. Zhao, H. B. Zhao, and L. Y. Chen, IEEE. Magn. Lett. **6**, 3500604 (2015).

[13] K. Gilmore, Y. U. Idzerda, and M. D. Stiles, Phys. Rev. Lett. **99**, 027204 (2007).

[14] M. Battiato, K. Carva, and P. M. Oppeneer, Phys. Rev. Lett. **105**, 027203 (2010).

[15] Y. Tserkovnyak, A. Brataas, and G. E. W. Bauer, Phys. Rev. B **66**, 224403 (2002).

[16] L. Frangou, S. Oyarzún, S. Auffret, L. Vila, S. Gambarelli, and V. Baltz, Phys. Rev. Lett. **116**, 077203 (2016).

[17] G. Malinowski, F. D. Longa, J. H. H. Rietjens, P. V. Paluskar, R. Huijink, H. J. M. Swagten, and B. Koopmans, Nat. Phys. **4**, 855 (2008).

[18] W. He, T. Zhu, X. Q. Zhang, H. T. Yang, and Z. H. Cheng, Sci. Rep. **3**, 2883 (2013).

[19] E. G. Tveten, A. Brataas, and Y. Tserkovnyak, Phys. Rev. B **92**, 180412(R) (2015).

[20] Y. Zhang, Q. Zhan, Z. Zuo, H. Yang, X. Zhang, G. Dai, Y. Liu, Y. Yu, J. Wang, B. Wang, and R.-W. Li, Phys. Rev. B **91**, 174411 (2015).
[21] R. L. Stamps, J. Phys. D: Appl. Phys. **33**, R247 (2000).
[22] F. D. Longa, Ph.D. thesis, Eindhoven University of Technology, The Netherlands, 2008.
[23] S. Iihama, Y. Sasaki, H. Naganuma, M. Oogane, S. Mizukami, and Y. Ando, J. Phys. D: Appl. Phys. **49**, 035002 (2016).
[24] K. C. Kuiper, T. Roth, A. J. Schellekens, O. Schmitt, B. Koopmans, M. Cinchetti, and M. Aeschlimann, Appl. Phys. Lett. **105**, 202402 (2014).
[25] B. Vodungbo, B. Tudu, J. Perron, R. Delaunay, L. Müller, M. H. Berntsen, G. Grübel, G. Malinowski, C. Weier, J. Gautier, G. Lambert, P. Zeitoun, C. Gutt, E. Jal, A. H. Reid, P. W. Granitzka, N. Jaouen, G. L. Dakovski, S. Moeller, M. P. Minitti *et al.*, Sci. Rep. **6**, 18970 (2016).
[26] M. van Kampen, C. Jozsa, J. T. Kohlhepp, P. LeClair, L. Lagae, W. J. M. de Jonge, and B. Koopmans, Phys. Rev. Lett. **88**, 227201 (2002).
[27] H. C. Yuan, S. H. Nie, T. P. Ma, Z. Zhang, Z. Zheng, Z. H. Chen, Y. Z. Wu, J. H. Zhao, H. B. Zhao, and L. Y. Chen, Appl. Phys. Lett. **105**, 072413 (2014).
[28] Y. Fan, X. Ma, F. Fang, J. Zhu, Q. Li, T. P. Ma, Y. Z. Wu, Z. H. Chen, H. B. Zhao, and G. Lupke, Phys. Rev. B **89**, 094428 (2014).
[29] R. D. McMichael, M. D. Stiles, P. J. Chen, and W. F. Egelhoff, J. Appl. Phys. **83**, 7037 (1998).
[30] S. M. Rezende, A. Azevedo, M. A. Lucena, and F. M. de Aguiar, Phys. Rev. B **63**, 214418 (2001).
[31] J. BeikMohammadi, J. M. Jones, S. Paul, B. Khodadadi, C. K. A. Mewes, T. Mewes, and C. Kaiser, Phys. Rev. B **95**, 064414 (2017).
[32] R. L. Rodríguez-Suárez, L. H. Vilela-Leao, T. Bueno, A. B. Oliveira, J. R. L. de Almeida, P. Landeros, S. M. Rezende, and A. Azevedo, Phys. Rev. B **83**, 224418 (2011).
[33] M. C. Weber, H. Nembach, B. Hillebrands, M. J. Carey, and J. Fassbender, J. Appl. Phys. **99**, 08J308 (2006).
[34] M. C. Weber, H. Nembach, B. Hillebrands, and J. Fassbender, J. Appl. Phys. **97**, 10A701 (2005).
[35] R. Arias and D. L. Mills, Phys. Rev. B **60**, 7395 (1999).
[36] H. S. Song, K. D. Lee, C. Y. You, S. H. Yang, S. Parkin, B. G. Park, J. W. Sohn, J. I. Hong, and S. C. Shin, Appl. Phys. E **8**, 053002 (2015).
[37] H. Moradi and G. A. Gehring, J. Magn. Magn. Mater. **256**, 3 (2003).
[38] H. Moradi, J. Magn. Magn. Mater. **278**, 317 (2004).
[39] T. Kato, Y. Matsumoto, S. Okamoto, N. Kikuchi, O. Kitakami, N. Nishizawa, S. Tsunashima, and S. Iwata, IEEE Trans. Magn. **47**, 3036 (2011).
[40] X. Ma, L. Ma, P. He, H. B. Zhao, S. M. Zhou, and G. Lüpke, Phys. Rev. B **91**, 014438 (2015).
[41] S. Azzawi, A. Ganguly, M. Tokaç, R. M. Rowan-Robinson, J. Sinha, A. T. Hindmarch, A. Barman, and D. Atkinson, Phys. Rev. B **93**, 054402 (2016).
[42] W. Zhang, M. B. Jungfleisch, W. J. Jiang, J. E. Pearson, A. Hoffmann, F. Freimuth, and Y. Mokrousov, Phys. Rev. Lett. **113**, 196602 (2014).
[43] S. Mizukami, F. Wu, A. Sakuma, J. Walowski, D. Watanabe, T. Kubota, X. Zhang, H. Naganuma, M. Oogane, Y. Ando, and T. Miyazaki, Phys. Rev. Lett. **106**, 117201 (2011).
[44] L. Jiang, J. Yang, H. Hao, G. Zhang, S. Wu, Y. Chen, O. Obi, T. Fitchorov, and V. G. Harris, Appl. Phys. Lett. **102**, 222409 (2013).
[45] M. Deb, E. Popova, M. Hehn, N. Keller, S. Mangin, and G. Malinowski, Phys. Rev. B **98**, 174407 (2018).
[46] B. Buford, P. Dhagat, and A. Jander, J. Appl. Phys. **115**, 17E309 (2014).
[47] P. He, X. Ma, J. W. Zhang, H. B. Zhao, G. Lupke, Z. Shi, and S. M. Zhou, Phys. Rev. Lett. **110**, 077203 (2013).
[48] P. Merodio, A. Ghosh, C. Lemonias, E. Gautier, U. Ebels, M. Chshiev, H. Béa, V. Baltz, and W. E. Bailey, Appl. Phys. Lett. **104**, 032406 (2014).
[49] Y. Liu, Z. Yuan, R. J. H. Wesselink, A. A. Starikov, and P. J. Kelly, Phys. Rev. Lett. **113**, 207202 (2014).
[50] Q. Liu, H. Y. Yuan, K. Xia, and Z. Yuan, Phys. Rev. Mater. **1**, 061401(R) (2017).
[51] M. Battiato, K. Carva, and P. M. Oppeneer, Phys. Rev. B **86**, 024404 (2012).
[52] V. P. Zhukov, E. V. Chulkov, and P. M. Echenique, Phys. Rev. B **73**, 125105 (2006).
[53] M. Fähnle, J. Seib, and C. Illg, Phys. Rev. B **82**, 144405 (2010).
[54] Y. W. Zhao, Y. Liu, H. M. Tang, H. H. Jiang, Z. Yuan, and K. Xia, Phys. Rev. B **98**, 174412 (2018).